

Detection of subsurface cavity structures using contact-resonance atomic force microscopy

Chengfu Ma^{1,2}, Yuhang Chen¹, Walter Arnold^{2,3}, and Jiaru Chu¹

¹Department of Precision Machinery and Precision Instrumentation, University of Science and Technology of China, Hefei, Anhui 230026, China

²I. Physikalisches Institut, Georg-August-Universität, Friedrich-Hund-Platz 1, D-37077 Göttingen, Germany

³Department of Materials Science and Technology, Campus D 2.2, Saarland University, D-66123 Saarbrücken, Germany

Corresponding author E-mail: chenyh@ustc.edu.cn

Abstract

To meet the surging demands for quantitative and nondestructive testing at the nanoscale in various fields, ultrasonic-based scanning probe microscopy techniques, such as contact-resonance atomic force microscopy (CR-AFM), have attracted increased attention. Despite considerable success in subsurface nanostructure or defect imaging, the detecting capabilities of CR-AFM have not been fully explored yet. In this paper, we present an analytical model of CR-AFM for detecting subsurface cavities by adopting a circular freestanding membrane structure as an equivalent cavity. The parameters describing the detection limits of CR-AFM for such structures include the detecting depth and the detectable area. These parameters are systematically studied for different cantilever eigenmodes for structures of different sizes and depths. The results show that the detecting depth depends on the structure size. The higher eigenmodes generally provide better detecting capabilities than the lower ones.

For an experimental verification, samples were prepared by covering **with HOPG flakes a polymethylmethacrylate (PMMA) substrate with open pores at its surface**. CR-AFM imaging on the HOPG-covered area **was** carried out using different eigenmodes in order to detect the pores in the PMMA. In addition, the influence of the applied tip load is also discussed.

Keywords: Contact-resonance atomic force microscopy; subsurface imaging; nondestructive testing; defect detection.

This is the author's peer reviewed, accepted manuscript. However, the online version of record will be different from this version once it has been copyedited and typeset.

PLEASE CITE THIS ARTICLE AS DOI: 10.1063/1.4981537

1. Introduction

Nondestructive subsurface imaging techniques on a nanoscale are of great importance in a wide range of fields. In material science, for example, the rapid development of composite materials based on the dispersion of nano-fillers into a matrix has created demands for characterization methods to quantitatively study the influence of the fillers on the physical properties of the composite. In biology, tracking the uptakes of living cells is fundamental for assessing the drug efficiency. Imaging of buried defects in nano-electronic devices is still a challenge. Conventional non-destructive subsurface testing methods, such as scanning acoustic microscopy, possesses a spatial resolution of no better than a few hundred nanometers according to the Rayleigh criterion. In addition, high-spatial resolution techniques, such as scanning electron microscopy or transmission electron microscopy, usually require destructive sample preparations in order to scan subsurface features.

By combining it with ultrasonic technology, atomic force microscopy (AFM) has been developed into a powerful tool for nanoscale nondestructive subsurface imaging in the past two decades. For example, ultrasonic force microscopy was first invented and used to image subsurface features in a graphite sample.¹ Then heterodyne force microscopy was introduced, and its analogues, such as scanning near-field ultrasound holography, were successfully applied to detect nanoparticles in a polymer substrate, buried voids in microelectronic structures, malaria parasite and the intake of nanoparticles in living cells.^{2,3} Especially contact-resonance atomic force microscopy (CR-AFM), including the so-called atomic force acoustic microscopy (AFAM) and ultrasonic atomic force microscopy (UAFM), are among the most promising techniques for realizing quantitative characterization. By recording the CR spectra of the cantilever while keeping the tip in contact with the sample surface and by subsequent analyzing with proper contact mechanics and cantilever dynamic models, CR-AFMs were used in quantitative mechanical characterization.⁴⁻¹⁰ There are also some reports of employing CR-AFM for subsurface imaging, such as the observation of subsurface dislocation in highly oriented pyrolytic graphite (HOPG), the adhesion mapping of a buried interface, and the detection of embedded nanostructures.¹¹⁻¹³

Even though much work has been carried out using analytical models by applying CR-AFMs in quantitative mechanical characterization, their subsurface detecting capabilities have not been fully explored yet. By now there are only a few papers published on this issue. For example, Yaralioglu *et al* proposed a radiation impedance based method in order to calculate the contact stiffness of layered materials in UAFM,¹⁴ which was further employed by Sarioglu *et al* in order to investigate the sensitivity of UAFM to interface defects in film/substrate structures.¹⁵ A 3D finite element analysis (FEA) model was used by Parlak and Degertekin to simulate the contact stiffness between an AFM tip and a substrate with buried nanostructures, and to theoretically investigate the influence of multiple subsurface structures, contact forces, and material properties in subsurface defect detection.¹⁶ Experimentally, Kimura *et al* employed various AFM techniques to elucidate the imaging mechanisms for deeply buried Au nanoparticles in a soft polymer.¹⁷ Striegler and co-workers fabricated well-defined subsurface reference structures to verify the detection capabilities of AFAM, and their results demonstrated that buried void structures at depths ranging from 180 nm to 900 nm, corresponding to up to ~10-times the contact radius of the tip, can be detected depending on the defect dimensions.¹⁸

In this paper we present an analytical model for detecting subsurface **cavities** or void structures by CR-AFM, which are a major type of defects in many advanced materials and

devices. By considering circular freestanding membrane structures as an equivalent for subsurface cavities, the detecting capabilities of CR-AFM for such structures were systematically studied. The detectable depth, the detectable area of the cavities for different cantilever eigenmodes and the influence of the applied tip load were theoretically investigated. Moreover, the detecting depth sensitivities for different cantilever eigenmodes were also discussed.

For an experimental verification, samples were prepared by covering with HOPG flakes the polymethylmethacrylate (PMMA) substrates that have open pores at the surface. When covered by the flakes, the open pore structure became subsurface cavities. CR-AFM imaging on the HOPG-covered areas was carried out for different eigenmodes and contact forces. The results show that the detecting depth depends on the structure's diameter. Deeper features can be detected by choosing higher eigenmodes and by applying larger contact forces.

2. Methods

2.1 Contact-resonance atomic force microscopy

A schematic of the CR-AFM system scanning a sample with subsurface cavity structures is illustrated in Fig. 1a. Ultrasonic excitations were applied via the signal generator to the piezo-shaker which vibrates the cantilever at its suspension (UA-FM mode) while the tip is in contact with the sample. The applied tip load is monitored and kept constant by the AFM feedback controller. The existence of subsurface features will alter the tip-sample contact stiffness, which will influence the cantilever oscillation. Thus, by extracting the amplitude, phase, and frequencies of the CR-AFM spectra, information of the subsurface cavity structures is obtained in images which are not visible in the topography image. A detailed description of the CR-AFM can be found elsewhere.¹⁹

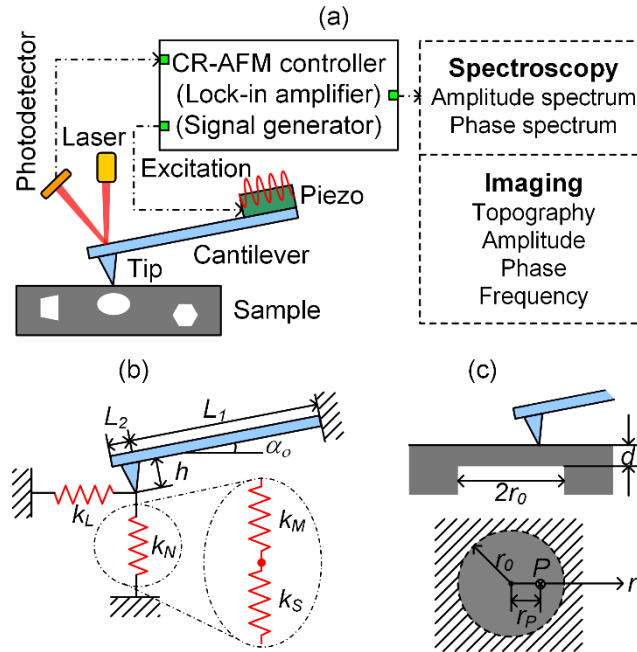


FIG. 1. (a) Schematic illustration of CR-AFM monitoring of a sample with subsurface cavity structures; (b) Mechanical model of the AFM cantilever in contact with the sample surface; (c) Equivalent model of subsurface cavities as edge-clamped circular free-standing membrane structures.

Our experiments were performed with a commercial AFM platform (MFP-3D Origin, Asylum Research, Santa Barbara, CA) using the UAFM mode. A ContAl-G cantilever (BudgetSensors, Innovative Solutions Bulgaria Ltd., Bulgaria) was employed. Prior to the measurements, the spring constant of the cantilever was determined to be 0.24 N/m by using the thermal calibration method.²⁰ The first four free resonance (FR) frequencies of the cantilever were measured to be respectively 14.7 kHz, 88.6 kHz, 244.9 kHz, and 481.3 kHz. UAFM imaging with different eigenmodes and contact forces was carried out.

2.2 Analytical models

Figure 1b shows a simplified equivalent model without damping of the vibrating cantilever in contact with the sample surface. Both the normal and the lateral contact forces are considered, represented by k_N and k_L , respectively. The cantilever has a total length of $L = L_1 + L_2$ from the clamped end to the free end, and the tip is located at position L_1 with the height h . Due to the mounting of the cantilever holder, a cantilever tilt of α_0 , which is usually between 11-15°, is also introduced in the model. The characteristic equation to describe the oscillation of an AFM cantilever based on the Euler-Bernoulli theory with the corresponding boundary conditions is well-known.^{19,6,10} Here, we only give the final equation in order to determine numerically the contact stiffness:

$$\frac{C}{3} \frac{k_C}{k_N} + B_1 + B_2 \frac{k_L}{k_N} + 3A \frac{k_L}{k_C} = 0, \quad (1)$$

where

$$A = \left(\frac{h}{L_1}\right)^2 (1 - \cos \lambda_n L_1 \cosh \lambda_n L_1)(1 + \cos \lambda_n L_2 \cosh \lambda_n L_2), \quad (2)$$

$$B_1 = \sin^2 \alpha_0 B_1^* - B_2^* + \cos^2 \alpha_0 B_3^*, \quad (3)$$

$$B_2 = \cos^2 \alpha_0 B_1^* + B_2^* + \sin^2 \alpha_0 B_3^*, \quad (4)$$

$$C = 2(\lambda_n L_1)^4 (1 + \cos \lambda_n L \cosh \lambda_n L), \quad (5)$$

with

$$B_1^* = \left(\frac{h}{L_1}\right)^2 (\lambda_n L_1)^3 [(1 + \cos \lambda_n L_2 \cosh \lambda_n L_2)(\sin \lambda_n L_1 \cosh \lambda_n L_1 + \cos \lambda_n L_1 \sinh \lambda_n L_1) - (1 - \cos \lambda_n L_1 \cosh \lambda_n L_1)(\sin \lambda_n L_2 \cosh \lambda_n L_2 + \cos \lambda_n L_2 \sinh \lambda_n L_2)], \quad (6)$$

$$B_2^* = \left(\frac{h}{L_1}\right)^2 (\lambda_n L_1)^2 \sin \alpha_0 \cos \alpha_0 [(1 + \cos \lambda_n L_2 \cosh \lambda_n L_2) \sin \lambda_n L_1 \sinh \lambda_n L_1 + (1 - \cos \lambda_n L_1 \cosh \lambda_n L_1) \sin \lambda_n L_2 \sinh \lambda_n L_2], \quad (7)$$

$$B_3^* = \lambda_n L_1 [(1 + \cos \lambda_n L_2 \cosh \lambda_n L_2)(\sin \lambda_n L_1 \cosh \lambda_n L_1 - \cos \lambda_n L_1 \sinh \lambda_n L_1) - (1 - \cos \lambda_n L_1 \cosh \lambda_n L_1)(\sin \lambda_n L_2 \cosh \lambda_n L_2 - \cos \lambda_n L_2 \sinh \lambda_n L_2)]. \quad (8)$$

Here, k_c is the spring constant of the cantilever and $\lambda_n L$ is the normalized wave number of the n -th flexural mode which can be related to the contact resonance frequency f_n^c and the free resonance frequency f_n^0 by the dispersion equation

$$(\lambda_n L)^c = (\lambda_n L)^0 \sqrt{\frac{f_n^c}{f_n^0}} = 1.8571 \sqrt{\frac{f_n^c}{f_1^0}}. \quad (9)$$

Thus, the relation between the normal contact stiffness and the CR frequency can be built analytically.

When the tip scans over subsurface cavities, deformations of the structure will be experienced besides local deformations of the material. This will alter the normal contact stiffness and thus the cantilever oscillation, and that is why subsurface cavities can be sensed. As quite small loads were applied, the material deformation and structure deflection can both be assumed to be elastic. Therefore, the normal contact stiffness k_N can be regarded as a series connection of the deflection stiffness k_S and the material deformation stiffness k_M as shown in Fig. 1b, that is $1/k_N = 1/k_S + 1/k_M$. According to the Hertz contact mechanics, the material deformation stiffness can be determined to be $k_M = (6E^* R F_N)^{1/3}$ where E^* is the reduced Young's modulus with $1/E^* = (1-\nu_t^2)/E_t + (1-\nu^2)/E$, R is the tip radius, and F_N is the applied normal tip load. Parameters E , E_t , ν , ν_t are the Young's modulus and the Poisson's ratios of the sample and the tip, respectively. The lateral contact stiffness k_L can be estimated to be $2(1-\nu)/(2-\nu)$ times of k_M .²¹

In the experiments the tip load F_N is kept constant and hence k_M and k_L should be constant during a measurement. As a consequence, the deflection stiffness k_S can directly be related to the CR frequencies. Additionally, k_S is determined by the structure and material properties of the cavity and the tip position.

Because the shapes of cavity structures are usually irregular, it is difficult to build corresponding equivalent models which reflect their stiffness. Here, we use an edge-clamped circular freestanding membrane as an equivalent model for the subsurface structure with a diameter of $2r_0$ and a thickness of d , respectively, representing the lateral dimension and its depth, see Fig. 1c. For a membrane with an eccentric point force P acting at a distance of r_P from its center, the maximum deflection can be expressed as:²²

$$w(r_P, 0) = \frac{P}{16\pi D} \frac{(r_0^2 - r_P^2)^2}{r_0^2}, \quad (10)$$

where $D = Ed^3/12(1-\nu^2)$ is the flexural rigidity of the membrane. Then, the membrane deflection stiffness can be expressed as $k_S(r_P, 0) = P/w(r_P, 0)$. For simplicity, no residual stress is taken into account which can be added in a later stage.¹⁰

2.3 Detecting capabilities

The analytical model described above relates the shifts of the measured CR frequencies on a circular freestanding membrane structure with its diameter and thickness (depth) and the

experimental parameters. We define a minimal detectable frequency shift Δf for our experimental set-up. Only when the CR frequency at the structure center shifts more than Δf from the substrate or bulk material, the subsurface structure becomes detectable. This also determines the detecting depth. Moreover, even though a structure is distinguishable when the cantilever tip is above its central axis, it does not mean that the whole structure can be sensed because the deflection stiffness of the structure will approach the stiffness of the bulk material at its edges. Therefore, the detectable area will be another important parameter in studying the detecting capabilities.

Here, we demonstrate an analytical evaluation of the two detecting capabilities. A conservative estimation of the CR frequency resolution $\Delta f = 1$ kHz is considered. To remain consistent with our verification experiments, a HOPG sample with a Young's modulus of 18 GPa and a Poisson's ratio of 0.25 is used in all our analytical calculations, with a tip load of 82 nN and a tip radius of 50 nm. The cantilever length is 450 μm , and the tip height is $h = 17$ μm with the ratio $L_t/L = 435/450$. The cantilever tilt is set to be $\alpha_0 = 11^\circ$. The Young's modulus and Poisson's ratio of the silicon tip are respectively 127 GPa and 0.278.

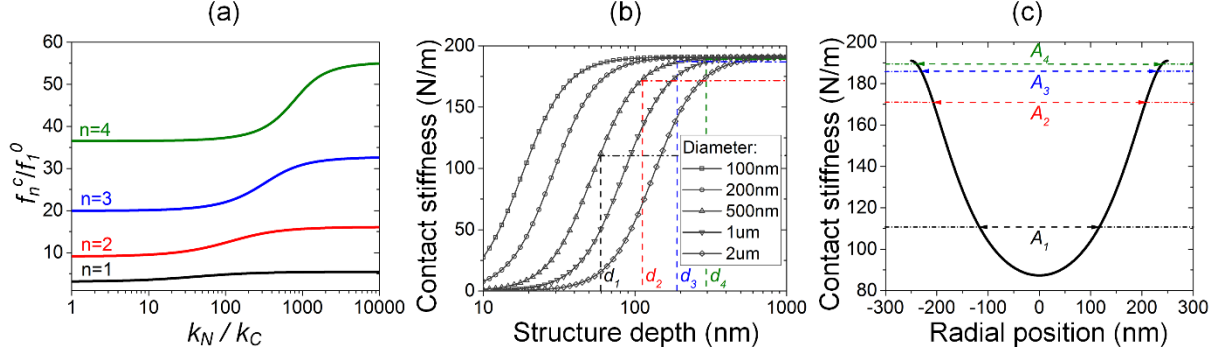


FIG. 2. (a) Relations between the normalized CR frequencies of the first four eigenmodes and the normalized contact stiffness; (b) Contact stiffness at the structure center as a function of depth for various diameters; (c) Contact stiffness of a 500 nm diameter structure at a depth of 50 nm versus radial position. The determination of the detecting depths (d_i) and the detectable widths (A_i) are indicated in (b) and (c).

From the contact model, the normal contact stiffness k_M on the bulk material was calculated to be about 191 N/m. So the lateral contact stiffness k_L was determined to be 164 N/m. The contact radius is estimated to be about 5.7 nm using Eq. (4.19) of Johnson.²³ According to Eq. 1, the relations between CR frequencies and the normal contact stiffness for the first four eigenmodes are shown in Fig. 2a, normalized to the first free resonance frequency and to the cantilever stiffness. For a contact-resonance frequency resolution of 1 kHz, the smallest detectable contact stiffness difference Δk_N is about 80.9 N/m, 19.5 N/m, 4.4 N/m and 1.4 N/m for the first four eigenmodes, respectively. Therefore, only when the contact stiffness at its center has a difference larger than these thresholds, can a subsurface cavity be detected. The relation between the contact stiffness at the structure's center and its thickness is shown in Fig. 2b for various diameters. It can be seen that the contact stiffness at the center approaches the value of the bulk material for a large structure depth. However, a rapid decrease of the contact stiffness can be found with decreasing depth. When we marked Δk_N on the stiffness versus structure depth curves, as illustrated for a diameter of 500 nm, the detecting depths d_1, d_2, d_3 , and d_4 can be determined for the first four eigenmodes, with larger detecting depths for higher eigenmodes.

Moreover, for a structure with a diameter of 500 nm and a depth of 50 nm, the normal contact stiffness distribution along its radial direction is shown in Fig. 2c. A rapid increase of the contact stiffness from the center to the periphery is found. By matching again with Δk_N , the detectable areas A_1 , A_2 , A_3 , and A_4 are determined for the first four eigenmodes with the higher eigenmodes showing larger detectable areas.

3. Results and Discussion

3.1 The effect of chosen eigenmodes

We investigated the detecting capabilities of the first four CR eigenmodes. As shown in Fig. 3a, detecting depths for subsurface cavity structures with different diameters were calculated. It can be seen that much deeper structures can be sensed if they are bigger in the horizontal dimension. In addition, the detecting depth of the CR-AFM can be much improved by applying higher eigenmodes, which opens the possibility of using multimode CR-AFM techniques for the tomographic reconstruction of subsurface void or cavity defects. Figure 3b depicts the detectable diameter ratios for structures with a diameter of 500 nm for various depths. There is a decrease of the detectable area for all eigenmodes with increasing depth. The increased sensitivity of the higher eigenmodes is again demonstrated with much larger detectable areas in comparison to the lower eigenmodes, and the advantages become more significant for deeper structures.

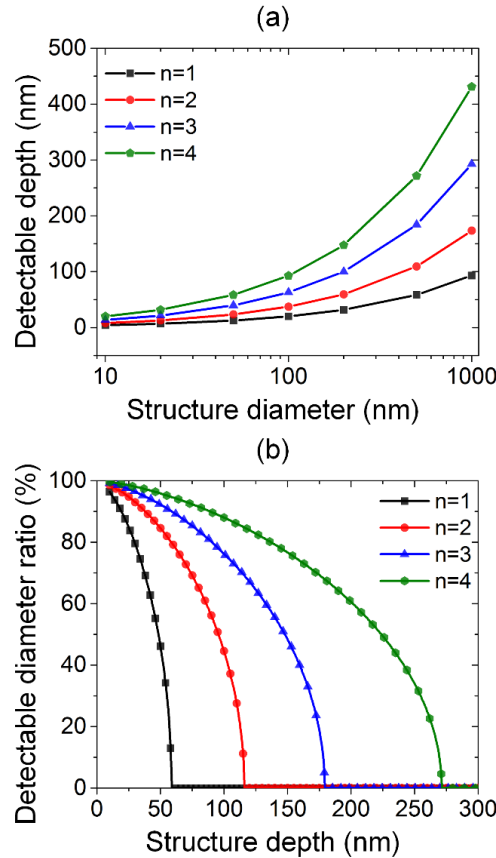


FIG. 3. Detecting capabilities of the first four CR eigenmodes: (a) Detecting depths for structures with different diameters; (b) Detectable diameter ratios for structures with a diameter of 500 nm and with various depths.

A more comprehensive study was carried out in which the detectable diameter ratios of the first four eigenmodes were calculated for structures with various diameters and depths. Figure 4 shows the results while the diameters and the depths were respectively up to 1000 nm and 500 nm. It should be mentioned that detecting depths for structures with certain diameters can also be acquired from Fig. 4, indicated by the contour line, where the detectable diameter ratio values turn to zero. The results illustrate a significant impact of the chosen CR eigenmodes on subsurface imaging for cavity structures, with larger detecting depths and more realistic visualization of the structures from the lateral dimensions by applying higher eigenmodes. Such maps can provide an easy-to-understand and comprehensive guide to evaluate the detecting capabilities of CR-AFM for subsurface cavity structures under certain settings.

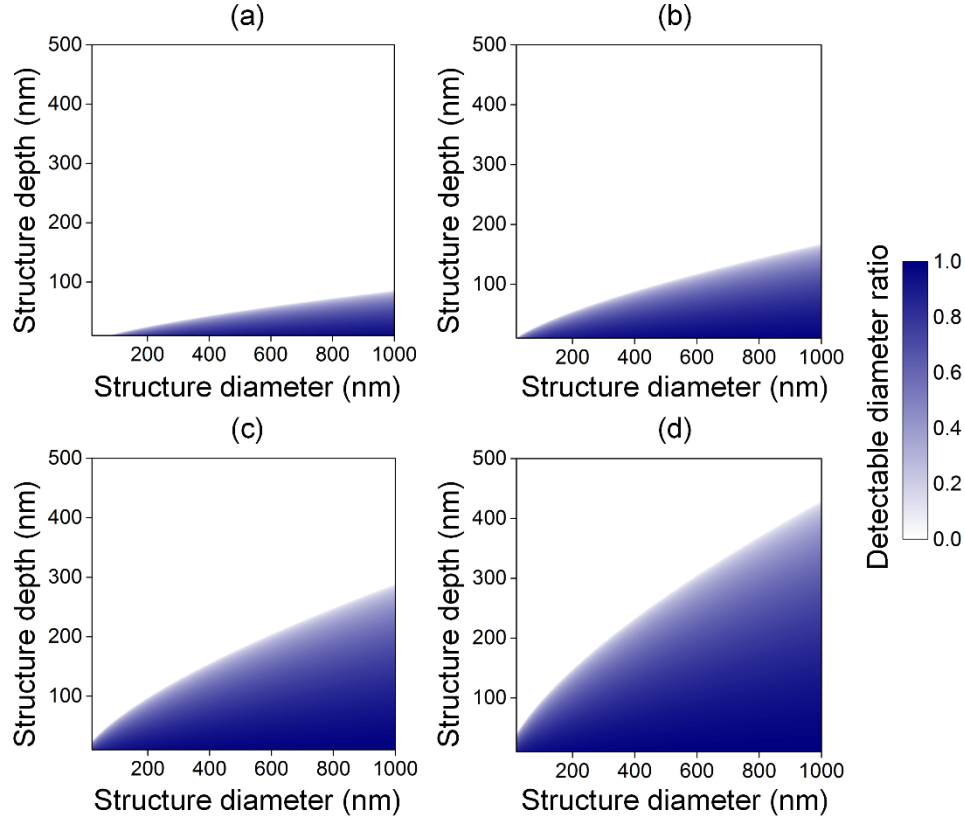


FIG. 4. Detectable diameter ratios for structures with various diameters, and (a)-(d) depths for the first four eigenmodes, respectively.

Furthermore, we evaluated and compared the depth detecting sensitivities of the first four eigenmodes. To this end, the CR frequency shifts induced by a unit depth change were calculated for various structure depths while the diameter was set to be 500 nm. The results are shown in Fig. 5 from which the maximal depth sensitivity can be discerned for each eigenmode which is the peak value. For the first four eigenmodes they are approximately 1.4, 3.2, 3.8, and 2.5 kHz/nm, respectively. In addition, depth sensitivity differences can be found between the first four eigenmodes, with each eigenmode having the best sensitivity with increasing structure depth.

This is analogous to the frequency sensitivity behavior of different eigenmodes for contact stiffness changes in CR-AFM as studied elsewhere.²⁴

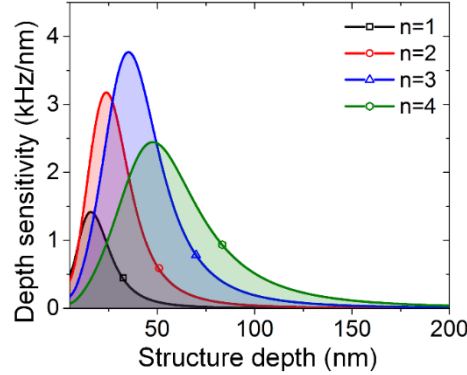


FIG. 5. Depth detecting sensitivities of the first four eigenmodes under various structure depths (diameter: 500 nm).

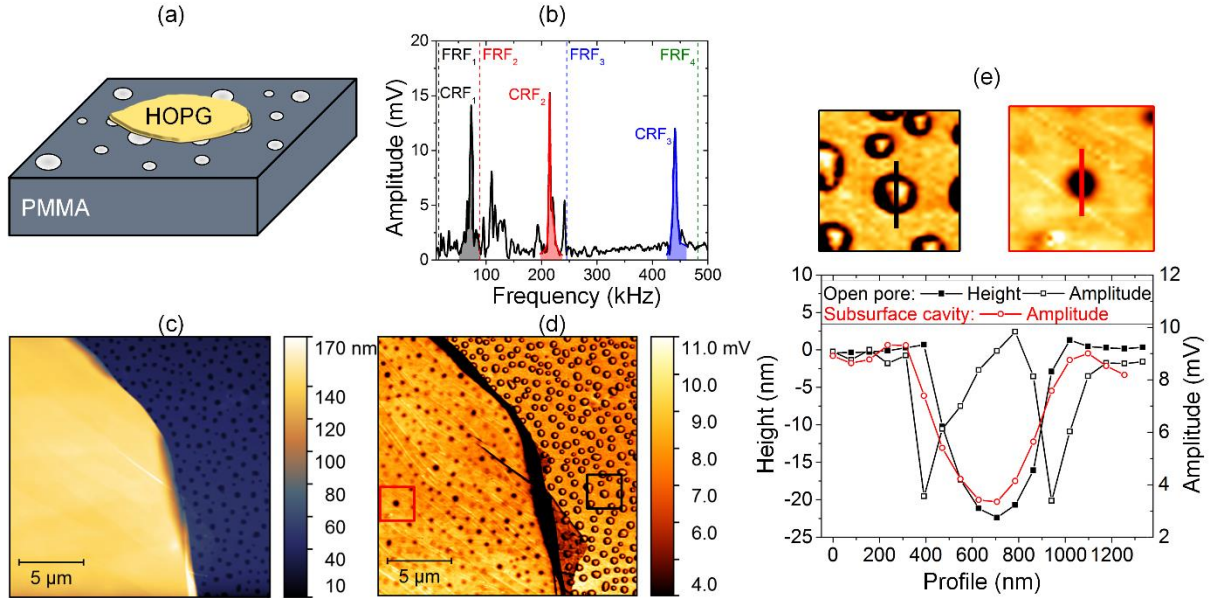


FIG. 6. (a) Schematic illustration of the scanned sample, prepared by covering a porous PMMA substrate with HOPG flakes. (b) CR amplitude spectrum obtained on the HOPG surface containing the first three eigenmodes with the first four FR frequencies marked by dashed lines; (c) AFM topography image on the flake and on the exposed PMMA substrate; (d) UAFM amplitude images on the same area as in (c) using a frequency of 440 KHz just below the contact-resonance frequency of 440.7 kHz; (e) Line-scans through two indications, one for subsurface cavity feature (in red) and one for an open pore (black open circles).

3.2 UAFM imaging

UAFM imaging experiments were carried out to verify our analysis. To this end, samples were first prepared by covering a porous PMMA substrate with HOPG flakes (see Fig. 6a). The investigated pores in the PMMA substrate have a mean diameter of approximately 503 nm, and HOPG flakes with three different thicknesses of about 102 nm, 65 nm and 33 nm are studied in

our experiments. Then, contact-resonance spectroscopy tests were conducted on one of the HOPG flakes to determine the CR frequencies. Figure 6b shows a typical amplitude spectrum over a range of 0 - 500 kHz for a tip load $P \approx 82$ nN for the first three CR frequencies of 73.0 kHz, 214.4 kHz, and 440.7 kHz. The first four FR frequencies are also shown. Finally, UAFM images were obtained on the HOPG flakes to examine the subsurface imaging capabilities for different eigenmodes and/or different tip loads. Figure 6c and Fig. 6d show respectively the obtained topography and UAFM amplitude images near a HOPG flake with the operation frequency set to be 440 kHz. The thickness of the HOPG flake was about 102 nm. It can be seen that the subsurface cavities below the HOPG flake are clearly revealed by the amplitude image but are not visible in the topography image. Neither the image contrast of the subsurface cavities nor the contrast of the open pores on the bare PMMA relate to their stiffness in a simple way. The amplitude images of the open pores on the bare PMMA are encircled by dark ring-like features located at the pore edges (Fig. 6e). Many of the subsurface cavities imaged through the flakes exhibit the opposite contrast. Such contrast inversions have been observed earlier and are caused by changes of the contact stiffness due to variations in elasticity, contact area, and by the operating frequency relative to the contact-resonance frequency.^{25,26,27} In addition, there are two “parasitic” fin-shaped multilayer graphene membranes around the flake edge having a thickness of about 4 nm. They can easily be distinguished in the UAFM images from the PMMA substrate and HOPG flake for their different elastic properties. We will concentrate our discussion on the main HOPG flake part hereafter.

To study the influence of the chosen eigenmodes experimentally, UAFM images with different operation frequencies of 72.3 kHz, 213.9 kHz, and 440.2 kHz around the first three CRs were obtained. The results are shown in Fig. 7. It can be seen from Fig. 7a that the UAFM image for the first eigenmode shows no features of the subsurface cavities. This indicates that the detecting depth of the first eigenmode is smaller than the HOPG flake’s thickness. However, by applying higher modes, the subsurface cavities are gradually revealed. From Figs. 7b and 7c, it can be seen that both the second and the third eigenmodes have large enough detecting depths. In addition, it is obvious that the third eigenmode gives a much clearer contrast and reveals smaller cavities than the second eigenmode.

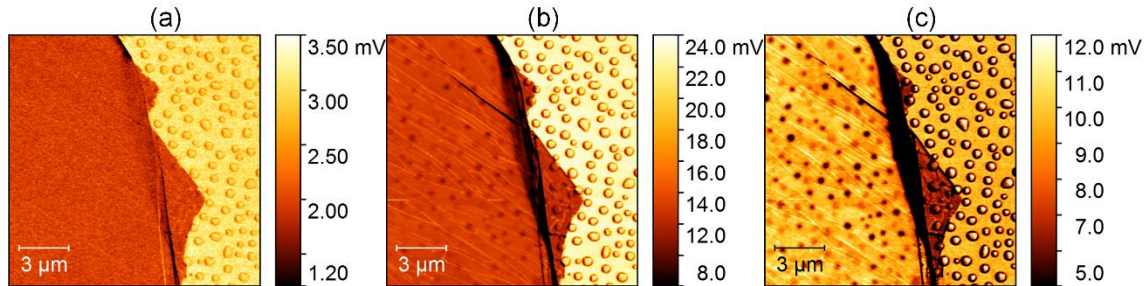


FIG. 7. UAFM amplitude images obtained for the first three eigenmodes. The corresponding operation frequencies are respectively (a) 72.3 kHz, (b) 213.9 kHz, and (c) 440.2 kHz.

A more detailed comparison between the obtained UAFM images of the first three eigenmodes is shown in Fig. 8a within the same scan area on the HOPG flake cropped from the amplitude images in Fig. 7. A topography crop of the PMMA substrate image is also displayed. Figure 8b displays the equivalent diameter histogram of the largest 25 cavities obtained on the PMMA substrate. The equivalent diameters of the cavities are in a range from about 409 nm to

637 nm and have a mean value of about 503 nm. Therefore, we conclude that the detecting depth of the first eigenmode is smaller than 102 nm for subsurface cavities with such dimensions, but that the second and third eigenmodes have larger detecting depths. Furthermore, we analyzed the imaging contrasts and the areas of the detected cavity features to make a quantitative comparison between the second and the third eigenmodes. To do so, the same 25 cavity features having the best contrasts were selected for both eigenmodes. Firstly, the UAFM amplitude contrast of the cavity features' centers from the HOPG bulk material were evaluated. The contrast or modulation depth $M = (A_{bulk} - A_{center}) / (A_{bulk} + A_{center})$ was determined, where A_{bulk} and A_{center} are amplitudes on the HOPG bulk material and the cavity center, respectively. The results are shown in Fig. 8c for the second and the third eigenmodes. A higher contrast or M can be found for the third eigenmode with a modulation depth of up to about 0.45, which is below that of 0.1 for the second eigenmode. Then, the apparent equivalent diameters of the detected features are evaluated and are shown in the histograms of Fig. 8d for both the second and the third eigenmodes. The results yield a clear difference between the two eigenmodes with mean values of about 420 nm and 470 nm for the second and the third eigenmodes, respectively. The third eigenmode still yields a better detecting contrast and gives precise dimensional information about the subsurface cavity structures.

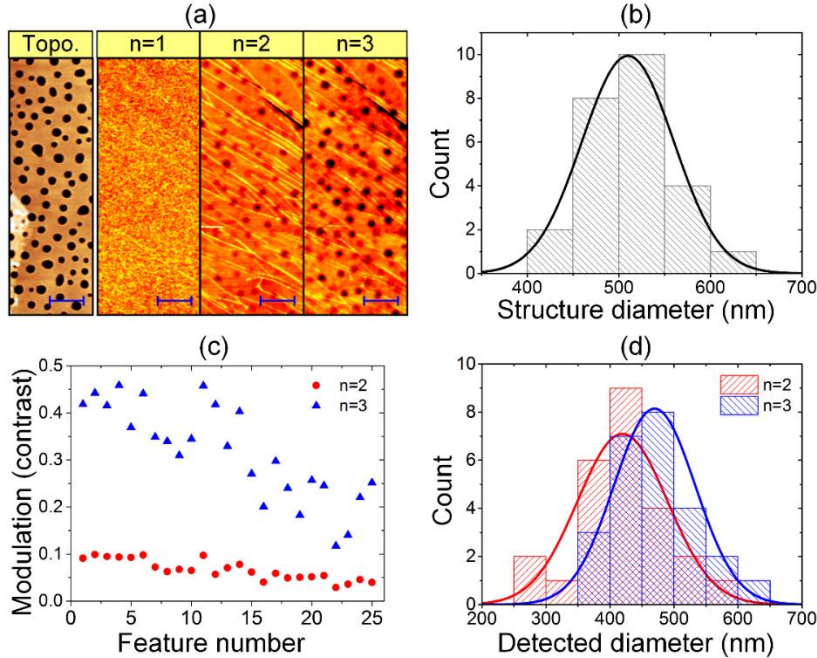


FIG. 8. (a) From left to right: topography on the uncovered PMMA substrate and UAFM amplitude images of the first three eigenmodes on the HOPG flake (scale bar: 2 μm); (b) Equivalent diameter histogram of the cavities on the PMMA substrate. (c) Modulation depth or contrast for different pores for the second and third eigenmodes; (d) Equivalent diameter histograms of the detected subsurface cavities for the second and third eigenmodes.

Here, quantitative comparisons between the experiments and our theoretical analysis are carried out. It should be mentioned that the effect of the PMMA substrate has little influence on the theoretical calculation. Although PMMA possesses an elastic modulus of 3 GPa, appreciably lower than the HOPG flakes (18 GPa), the effective elastic modulus of the HOPG flakes-PMMA

substrate system is, for a contact-radius to thickness ratio of about 0.06 and a modulus ratio $E_{\text{PMMA}}/E_{\text{HOPG}} \approx 0.2$ as in our case, at most 11% lower than flakes alone according to Perriot *et al.*²⁸ Therefore, the substrate effect are omitted in our calculations. When the same parameters were used in the theoretical analysis as in the experiments, we obtained detecting depths of about 51 nm, 104 nm, and 182 nm respectively for the first three eigenmodes, for subsurface cavities with a mean diameter of 503 nm. For such cavities with a depth of 102 nm, the analytically detectable diameters of the second and third eigenmodes will be around 83 nm and 374 nm, respectively. It can be found that even though differences between the theoretical and the experimental results exist, our theoretical analysis still gives good evaluations of the CR-AFM's detecting capabilities for subsurface cavity structures. There are mainly two reasons for the differences: (1) A conservative frequency sensitivity Δf of 1 kHz is used in our calculations. This will cause an underestimate of the detecting depths and the detectable areas in comparison to a real system which possesses a smaller frequency sensitivity; (2) The equivalent diameters of the subsurface cavities were statistically obtained from the topography of a different area. This will also lead to underestimates when larger subsurface cavities exist in the tested area covered by the HOPG flake.

3.3 Influence of the applied load

The applied load or contact force is another important parameter besides the eigenmodes in the set-up, which can be tuned to improve the detecting capabilities. Here, we examined its influence on detecting subsurface cavity structures by both theoretical evaluation and experimental demonstration. Figure 9a shows the calculated detecting depths of the first eigenmode under various tip loads for subsurface cavity structures with a diameter of 500 nm. It can be seen that the influence of the applied load on the detecting depth is significant only when small loads are applied. In our calculation the detecting depth increases with increasing applied load up to about 400 nN. Then, the detecting depth gradually levels off with increasing load. In addition, when compared with the results for the higher eigenmodes (Fig. 3a), it can be concluded that the selected eigenmode has a larger influence on the detecting depth than the applied load. Thus, to obtain a better detecting depth for subsurface cavity structures, applying a relatively large tip load will not help much. In contrast, exploiting a higher mode will be a better idea.

Figure 9b shows a topography image of another HOPG flake with some folded layers on the upper part and some graphene membrane around it. The heights of the main HOPG flake are approximately 33 nm and 65 nm on the substrate part (Area I) and on the folded area (Area II). Then, UAFM images were obtained for the first eigenmode with different tip loads. The amplitude images for loads of $F_N = 77$ nN and $F_N = 153$ nN are shown in Fig. 9c and Fig. 9d, respectively. Only a small amount of very blurry cavity features can be seen on area I for the smaller load. However, many cavity features are clearly revealed all over area I for the larger load, demonstrating the influence of the applied load on the detecting depth in accordance with our theoretical analysis.

Figure 9b shows a topography image of another HOPG flake with some folded layers on the upper part and some graphene membrane around it. The heights of the main HOPG flake are approximately 33 nm and 65 nm on the substrate part (Area I) and on the folded area (Area II). Then, UAFM images were obtained for the first eigenmode with different tip loads. The amplitude images for loads of $F_N = 77$ nN and $F_N = 153$ nN are shown in Fig. 9c and Fig. 9d, respectively. Only a small amount of very blurry cavity features can be seen on area I for the

smaller load. However, many cavity features are clearly revealed all over area I for the larger load, demonstrating the influence of the applied load on the detecting depth in accordance with our theoretical analysis.

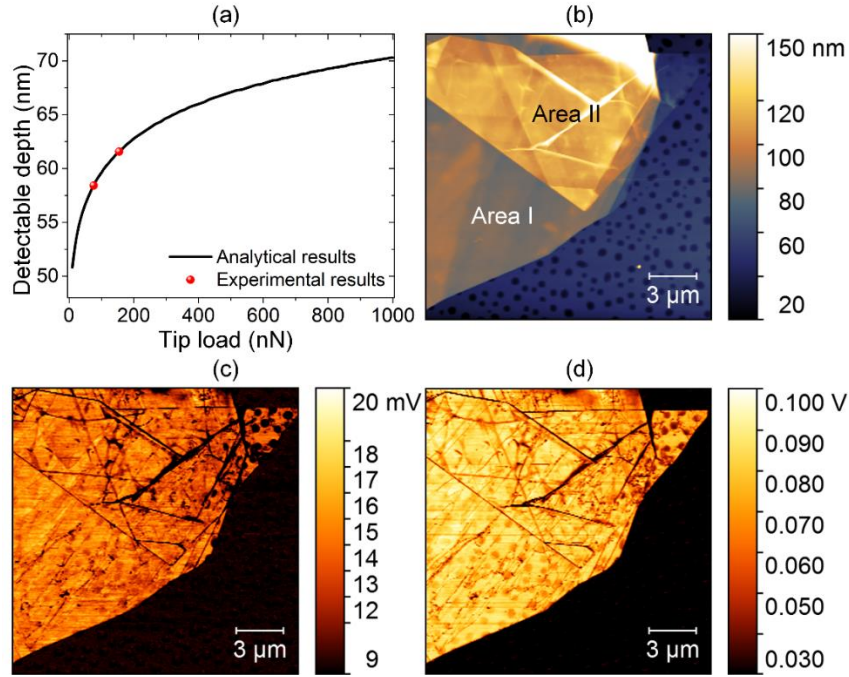


FIG. 9. (a) Detecting depths of the first eigenmode under various tip loads for subsurface cavities with a diameter of 500 nm in HOPG; (b) Topography around a HOPG flake on the PMMA substrate; (c) and (d) UAFM amplitude images using the first eigenmode under tip loads of $F_N = 77$ nN and $F_N = 153$ nN, respectively.

4. Conclusions

By considering subsurface cavity structures as circular freestanding membrane structures, an analytical model of CR-AFM for detecting subsurface void structures was proposed. Based on the model, the detecting capabilities including the detecting depth and the detectable area of CR-AFM were systematically studied. As an experimental verification, UAFM mapping was applied to image subsurface cavity structures on a PMMA substrate covered by HOPG flakes.

Firstly, the influence of the selected eigenmodes was studied by evaluating the detecting depths and detectable areas for subsurface cavity structures with various depths and diameters. The results show that the detecting depths depend on the structure diameters. For cavities of the same diameter, larger detecting depths can be obtained with higher eigenmodes. Higher eigenmodes provide also larger detectable areas for structures having the same diameter and depth. In addition, the detecting depth sensitivities of different eigenmodes were also discussed, indicating a promising prospect of using multimode CR-AFM techniques for tomographic reconstruction of subsurface voids and cavities in different depths. Then, the influence of the applied load on the detecting depth was investigated and it was found to become significant only when small loads were applied. It was found that the employed eigenmode determines the detecting depth to a larger extent than the applied load. Finally, experimental UAFM images

gave good agreement with the theoretical analysis. The influence of both the chosen eigenmode and the applied load were well demonstrated.

Acknowledgements

This research work was financially supported by the National Natural Science Foundation of China (reference numbers 51275503 and 51675504). Chengfu Ma gratefully acknowledges the China Scholarship Council for support.

References

- ¹ K. Yamanaka, H. Ogiso and O. Kolosov, *Appl. Phys. Lett.* **64**, 178-180 (1994).
- ² G. S. Shekhawat and V. P. Dravid, *Science* **310**, 89-92 (2005).
- ³ L. Tetard, A. Passian, R. H. Farahi and T. Thundat, *Ultramicroscopy* **110**, 586-591 (2010).
- ⁴ U. Rabe, S. Amelio, E. Kester, V. Scherer, S. Hirsekorn and W. Arnold, *Ultrasonics* **38**, 430-437 (2000).
- ⁵ D. C. Hurley, M. Kopycinska-Müller, A. B. Kos and R. H. Geiss, *Meas. Sci. Technol.* **16**, 2167 (2005).
- ⁶ D. C. Hurley and J. A. Turner, *J. Appl. Phys.* **102**, 033509 (2007).
- ⁷ H. Wagner, D. Bedorf, S. Küchemann, M. Schwabe, B. Zhang, W. Arnold and K. Samwer, *Nat. Mater.* **10**, 439-442 (2011).
- ⁸ A. B. Churnside, R. C. Tung and J. P. Killgore, *Langmuir* **31**, 11143-11149 (2015).
- ⁹ M. Kopycinska-Müller, A. Clausner, K. B. Yeap, B. Köhler, N. Kuzeyeva, S. Mahajan, T. Savage, E. Zschecha and K. J. Wolter, *Ultramicroscopy* **162**, 82-90 (2016).
- ¹⁰ C. Ma, Y. Chen, J. Chen and J. Chu, *Appl. Phys. Express* **9**, 116601 (2016).
- ¹¹ T. Tsuji and K. Yamanaka, *Nanotechnology* **12**, 301 (2001).
- ¹² D. C. Hurley, M. Kopycinska-Müller, E. D. Langlois, A. B. Kos and N. Barbosa, *Appl. Phys. Lett.* **89**, 1911 (2006).
- ¹³ J. P. Killgore, J. Y. Kelly, C. M. Stafford, M. J. Fasolka and D. C. Hurley, *Nanotechnology* **22**, 175706 (2011).
- ¹⁴ G. G. Yaralioglu, F. L. Degertekin, K. B. Crozier and C. F. Quate, *J. Appl. Phys.* **87**, 7491-7496 (2000).
- ¹⁵ A. F. Sarioglu, A. Atalar and F. L. Degertekin, *Appl. Phys. Lett.* **84**, 5368-5370 (2004).
- ¹⁶ Z. Parlak and F. L. Degertekin, *J. Appl. Phys.* **103**, 114910 (2008).
- ¹⁷ K. Kimura, K. Kobayashi, K. Matsushige and H. Yamada, *Ultramicroscopy* **133**, 41-49 (2013).
- ¹⁸ A. Striegler, B. Koehler, B. Bendjus, M. Roellig, M. Kopycinska-Mueller and N. Meyendorf, *Ultramicroscopy* **111**, 1405-1416 (2011).
- ¹⁹ U. Rabe, M. Kopycinska-Müller and S. Hirsekorn, in *Acoustic Scanning Probe Microscopy*, edited by F. Marinello, D. Passeri and E. Savio (Springer, Berlin, Heidelberg, 2013) pp. 123-153.
- ²⁰ J. E. Sader, J. W. Chon and P. Mulvaney, *Rev. Sci. Instrum.* **70**, 3967-3969 (1999).
- ²¹ P. E. Mazeran and J. L. Loubet, *Tribol. Lett.* **7**, 199-212 (1999).
- ²² R. Szilard, in *Theories and applications of plate analysis: classical numerical and engineering methods*, (John Wiley & Sons, Inc., Hoboken, New Jersey, 2004) pp. 161-165.
- ²³ K. L. Johnson, in *Contact mechanics*, (Cambridge University Press, Cambridge, 1987) pp. 84-106.
- ²⁴ J. A. Turner and J. S. Wiehn, *Nanotechnology* **12**, 322 (2001).
- ²⁵ C. Ma, Y. Chen and T. Wang, *AIP Adv.* **5**, 027116 (2015).
- ²⁶ U. Rabe, S. Amelio, M. Kopycinska S. Hirsekorn, M. Kempf, M. Göken, and W. Arnold, *Surface and Interface Analysis* **33**, 65-70 (2002).
- ²⁷ T. Tsuji, H. Ogiso, J. Akedo, S. Saito, K. Fukuda, and K. Yamanaka, *Jap. J. Applied Physics*, **43**, 2907 (2004).
- ²⁸ A. Perriot and E. Barthel, *J. Mater. Res.* **19**, 600-608 (2004).